Power Decoupling Control for V2G/G2V/PV2G Operation Modes in Single-Phase PV/Battery Hybrid Energy System With Low DC-Link Capacitance

ZHIGANG ZHANG[1], BIN LIU [ID][2], AND SHAOJIAN SONG[2]

[1]School of Management Science and Engineering, Guangxi University of Finance and Economics, Nanning 53007, China
[2]School of Electrical Engineering, Guangxi University, Nanning 530004, China

Corresponding author: Bin Liu (bingo.liu@gxu.edu.cn)

ABSTRACT Three-port intelligent conversion systems, interfacing photovoltaic (PV) arrays and electric vehicles (EVs), with an electrical grid, are a promising flexible infrastructure for future smart grids. In this system, multi-energy, direct current (DC), and alternating current (AC) power are decoupled by a larger DC-link capacitor. However, bulk capacitors prevent the achievement of high power density and high reliability of this system. To address this issue, active power decoupling control for a single-phase three-port conversion system is proposed in this paper. Owing to its low internal impedance, the inherent double-line-frequency ripple power in a single-phase system can be actively absorbed by a Li-ion battery pack, with a sinusoidal charging/discharging technique, in the proposed control strategy. Therefore, the capacitance of the DC-link capacitors can be significantly reduced. Further, a DC-link voltage ripple resonant compensation control loop was developed to ensure single-phase ac power quality on the grid side. Finally, the experimental results obtained from a 2.5 kVA single-phase three port power conversion prototype verify the feasibility and performance of the proposed control strategies.

INDEX TERMS Single-phase photovoltaic/battery energy system, three-port converter, power decoupling, dc-link voltage ripple suppress.

I. INTRODUCTION

The smart grid, as an emerging form of urban power grid, offers an opportunity for customers to take an active part in the electric markets [1], [2]. On the other hand, grid-connected plug-in EVs, which are grid-connected PV systems, can be leveraged to provide valuable grid services [3], [4] when they are managed via an intelligent conversion system. Therefore, a three-port integrated hybrid energy conversion system, which interfaces EVs and PV, with an electrical grid, and promises to admit renewable energy integration and intelligent energy management at high efficiency and reliability [5], has drawn increasing attention.

As EVs are typically charged or discharged at several kilowatts [6], the PV/battery hybrid energy system commonly

interacts with a single-phase grid. In a simplified configuration of the PV/battery hybrid system, the power flows among the batteries in EVs, PV arrays, and the grid, along with the interconnection between the three-port conversion system (hereinafter referred to as TPCS), as shown in Fig.1. The interconnection can be performed through four different operation modes under the frame of the smart grid:

1) PV2G operation mode: The DC energy produced by the PV arrays is converted to AC energy and injected into the single-phase grid.
2) V2G operation mode: DC energy from EVs is discharged to the grid, providing ancillary services to the grid.
3) G2V operation mode: EVs batteries are charged by AC energy from the grid.
4) PV2V operation mode: EV batteries are charged by DC energy, which is produced by the PV arrays.

The associate editor coordinating the review of this manuscript and approving it for publication was Tariq Masood [ID].
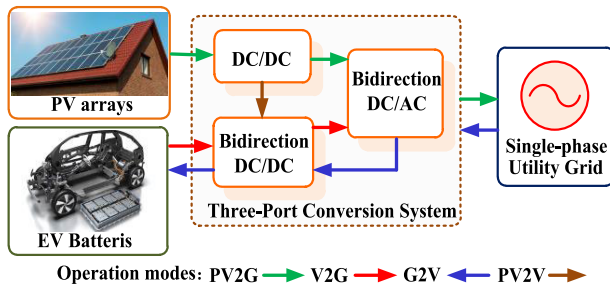
FIGURE 1. Schematic diagram of the PV/battery hybrid system and its operation modes.

Among the aforementioned operation modes, the inherent double-line-frequency power pulsation on the grid side of the TPCS may have negative effects on the PV/battery hybrid system. These negative effects, such as voltage fluctuation in the DC-link, distortion in AC current of TPCS, reduced life expectancy of dc capacitors, and reduction in efficiency, reliability, and stability of the entire system [7], [8]. In particular, as multiple energy flows and multiple operating modes consist of TPCS, the power-coupling problem becomes complex. Consequently, there is an urgent need to study appropriate power-decoupling control strategies for TPCS.

To mitigate or eliminate double-line-frequency ripple power, various power decoupling topologies and control algorithms have been presented in the literature. Increasing the capacitance of the DC-link capacitor is a straightforward and valid solution for ripple power decoupling, which was reported in [9], [10]. However, a larger dc-link capacitor leads to a lower power density, and the requirement of larger electrolytic capacitors contradicts the high reliability and long lifetime requirement. Moreover, the size and price of the capacitor depend on the capacitance. Thus, a capacitor with a higher capacitance is much more expensive and bulky. Therefore, several active decoupling techniques have been proposed recently. Generally, these active decoupling methods can be classified into two main categories: (1) adding active auxiliary circuits, such as [11]–[15] and (2) modifying the conventional control algorithms or modulation methods, such as [16], [17]. Refs [11], [12] adopted a symmetrical half-bridge circuit and utilized dc-link capacitors to absorb ripple power. By doing so, a capacitance reduction was achieved. Ref [13] adopted a full-bridge-type active power decoupling circuit to ensure high efficiency and accuracy for maximum power point tracking in a single-phase PV inverter. Refs [14], [15] used a buck converter supplied by a third winding of the transformer to generate the necessary ripple cancelation demanded by the DC side. From the perspective of active power decoupling modulation and control, Ref [16] analyzed the harmonics caused by the voltage ripple in an inverter with a feedback control, and derived a closed-form solution to calculate the amplitude of the ripple-caused harmonics for harmonic-free modulation. By adopting double-channel current feedback, Ref [17] forces all ripple power

absorbed through the DC-link capacitor, and thus achieves the objective of ripple-free input current.

In the above studies, the ripple power is absorbed by active auxiliary circuits or passive components, DC-link capacitors, or input inductors, but the latter results in an increase in the input current ripple or DC-link voltage ripple. Specifically, for the case of a TPCS in a PV/battery hybrid energy system, PV arrays are unsuitable for decoupling the ripple power owing to their high impedance characteristics. Meanwhile, large-capacity electrolytic capacitors should be avoided to reduce the system volume and cost. Moreover, to achieve high stability under steady-state operation, a rapid transient response, high AC power quality, and low DC-link voltage ripple should be promised [18], [19]. In fact, supposing the ripple energy absorbed by the batteries alternatively, the dc-link capacitance can be significantly reduced, and minor impacts on temperature rise are brought [20], [21]. Sinusoidal ripple current charging (SRCC) has been reported to increase both the charging efficiency and energy efficiency in batteries [22]; however, studies on employing the sinusoidal charging/discharging technique to achieve the power decoupling function for the TPCS are lacking.

Based on the synthesis of the SRCC scheme and an in-depth analysis of the ripple power balance, a novel power decoupling control strategy is proposed. In contrast to the existing literature, Li-ion batteries are specially selected for power decoupling components, based on the AC equivalent impedance model, and the analysis of different characteristics of the PV array and Li-ion battery. With a finely designed sinusoidal charging scheme and additional direct control path on the DC-link voltage ripple, the proposed power decoupling method can be effectively applied in V2G/G2V/PV2G operation modes in single-phase TPCS. To this end, the frequency of SRCC is specially tuned in double-line frequency; thus, the ripple power can be absorbed with much less dc-link capacitance. Moreover, this study analyzes the power flow and ripple power of the TPCS in terms of power conservation and power balance. Finally, comprehensive experimental results obtained from the two-stage TPCS prototype are presented to verify the performance of the proposed method.

II. ANALYSIS OF THE RIPPLE POWER FLOW AND THE SELECTION OF DECOUPLING COMPONENT FOR SINGLE-PHASE PV/BATTERY HYBRID SYSTEM
A. TOPOLOGY OF THE TWO-STAGE THREE-PORT SINGLE-PHASE PV/BATTERY HYBRID SYSTEM

A bidirectional half-bridge dc/dc converter (buck-boost converter) is used to interface with the batteries in EVs, and the boost converter is used to interface the PV arrays. L_{PV} denotes the boost inductor, and u_{PV} and i_{PV} denote the input voltage and input current of the boost converter on the PV side, respectively. L_B denotes the inductor of the bidirectional half-bridge dc/dc converter, and u_B and i_B denote the input voltage and input current of the buck-boost converter, respectively. It is worth mentioning that, in this hybrid energy system, the
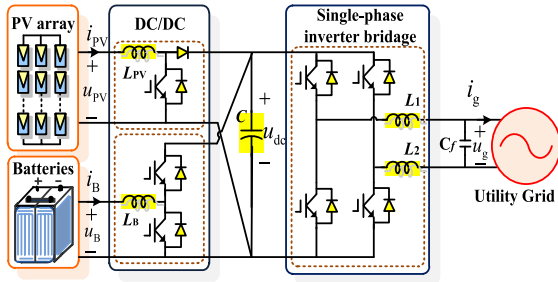
FIGURE 2. Topology of the two-stage three-port single-phase PV/battery hybrid energy system.

three converters are integrated in a single DC-link capacitor C, maintaining the characteristics of each converter. The AC filter is composed of inductors L_1, L_2, and capacitors C_f, u_g is the grid voltage, and i_g is the grid current injected by the PV/battery hybrid energy system.

B. GENERATION AND PROPAGATION MECHANISM OF RIPPLE POWER

Based on the instantaneous power theory, the generation mechanism of ripple power on the grid side of a single-phase PV/battery hybrid system can be studied analytically. Considering the operation modes of V2G, G2V, and PV2G, TPCS usually provides reactive power to the grid; therefore, the angle of the grid current i_g laying behind the grid voltage u_g is assumed to be φ. Thus, the instantaneous values of the grid voltage and grid current can be written as:

$$u_g = U_g \sin (\omega t), \tag{1}$$

$$i_g = I_g \sin (\omega t - \varphi), \tag{2}$$

where U_g and I_g denote the grid voltage and grid current amplitudes, respectively, and ω describes the fundamental angular frequency of the grid. If the reactive power is considered, the instantaneous power from the grid, p_g, can be written as:

$$
\begin{aligned}
p_g = u_g i_g &= U_g \sin (\omega t) I_g \sin (\omega t - \varphi) \\
&= \frac{1}{2} U_g I_g \cos \varphi - \frac{1}{2} U_g I_g \cos (2\omega t - \varphi) \\
&= p_d + p_r.
\end{aligned}
\tag{3}
$$

Equation (3) shows that there are dc power and ac double-line-frequency ripple power in the grid, presented by the first and second items on the right-hand side of (3). These can be defined as p_d and p_r, respectively. Supposing that p_{pv} and p_B are the instantaneous power in the PV array side and battery side, respectively, and assuming that there is no power loss in the TPCS, the grid power p_g is equal to the sum of p_{pv} and p_B, in the direction definition in Fig.2, namely:

$$p_g = p_{PV} + p_B. \tag{4}$$

In the operation modes of V2G, G2V, and PV2G, the ripple power should be absorbed by the intermediate dc-link in TPCS, as the sum of p_{pv} and p_B is the direct current. Consequently, the pulsating power can propagate to the DC-link,

PV arrays, or batteries, leading to a double-line-frequency voltage ripple in the DC-link voltage u_{dc}, or current ripple in the input current i_{PV}, i_B on the PV or EV side, respectively. Assuming that the dc-link voltage u_{dc} is approximated by its mean value U_0, u_{dc} can be derived as:

$$u_{dc} = U_0 + u_r, \tag{5}$$

where u_r is the voltage ripple in the DC-link. Assuming the pulsating power p_r absorbed by the DC-link capacitors, it can be expressed as [23]:

$$Cu_{dc} \frac{du_{dc}}{dt} = p_r = -\frac{1}{2} U_g I_g \cos (2\omega t - \varphi). \tag{6}$$

By performing integration on both sides of equation (6) and omitting the second-order item, u_r can be derived as:

$$u_r = \frac{U_g I_g}{4\omega C U_0} \sin (2\omega t - \varphi). \tag{7}$$

On the other hand, assuming that the ripple power p_r is absorbed by the input inductor L_{PV} or L_B, in the front-end dc/dc converters completely, the current ripple i_{rPV} and i_{rB}, which are superposed into the PV input current i_{PV} and battery input current i_B, respectively, can be derived as [24]:

$$i_{rPV} = \frac{U_g I_g}{4\omega L_{PV} I_{PV0}} \sin (2\omega t - \varphi), \tag{8}$$

$$i_{rB} = \frac{U_g I_g}{4\omega L_B I_{B0}} \sin (2\omega t - \varphi), \tag{9}$$

respectively. where I_{PV0} is the mean value of the input current i_{PV}, and I_{B0} is the mean value of the input current i_B.

From (7), (8), and (9), it is observed that a much higher value of capacitors or inductors is required when employing passive solutions to absorb the ripple power.

C. THE SELECTION OF RIPPLE POWER DECOUPLING COMPONENT

To develop the active decoupling method, a decoupling component should be selected with careful consideration. Based on the analysis of ripple power flow and the topology of the TPCS, the inherent double-line-frequency ripple power can be decoupled by three passive components: DC-link capacitors, PV arrays, and battery packs in EVs. This subsection describes the selection of the optimal decoupling component. Large electrolytic DC-link capacitors are direct decoupling components; however, the lifetime of such capacitors is usually limited and may compromise the system reliability [25]. Therefore, batteries in EVs and PV arrays are considered to be a ripple power decoupling component. Before selecting the optimal decoupling component, the impedance characteristics of the PV arrays and battery packs should be analyzed first.

In the front-end dc/dc, to decouple the ripple power and reduce the voltage ripple in the DC link, the ripple component in the input current i_{PV} or i_B, which is propagated from the back-end inverter, should be amplified. Generally, the current ripple i_r, caused by the coupling ripple power, can be

(a)

(b)

(c)
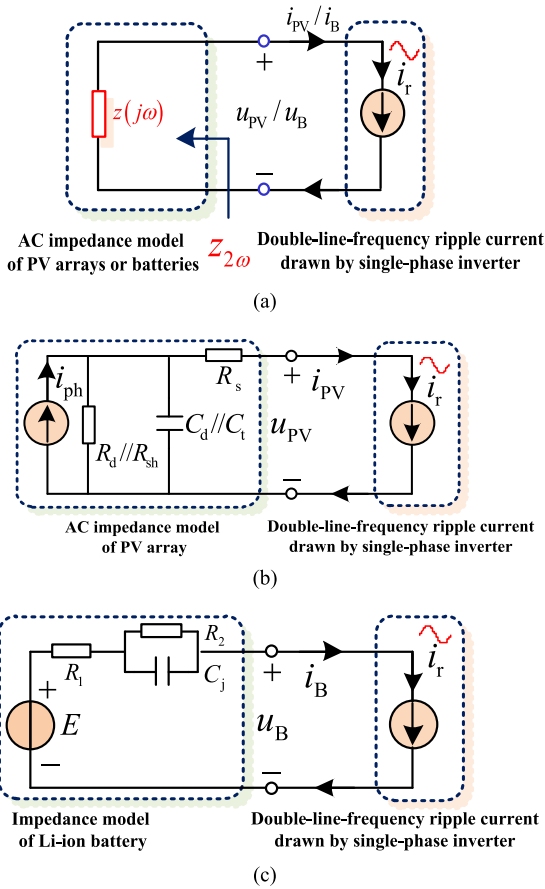
FIGURE 3. Equivalent circuits under different power conditions: (a) equivalent model of propagation circuit for the current ripple, (b) ac impedance equivalent circuit of PV arrays, (c) ac impedance equivalent circuit of Li-ion battery pack.

equivalent to a current source in an equivalent propagation circuit. Assuming $z(j\omega)$ as the ac impedance of PV arrays or Li-ion batteries, the magnitude $Z_{2\omega}$ of $z(j\omega)$ at double-line-frequency 2ω determines the value of the current ripple propagated into the input terminal, as shown in Fig.3(a).

Fig.3(b), Fig.3(c) show the ac impedance model of the PV arrays and Li-ion batteries, respectively. In the small signal model of the PV arrays, the diode is modeled in the circuit by R_d (dynamic resistance) and R_{sh} (shunt resistance) connected in parallel, C_d (diffusion capacitance) and C_t (transition capacitance) connected in parallel. R_d is a resistance showing the nonlinear characteristics of the diode. C_t is a capacitance from the space charge existing in the depletion layer of the PN junction. C_d is a capacitance proportional to the amount of the minority. Assume

$$R_P = R_d//R_{sh}, \tag{10}$$

$$C_P = C_d//C_t, \tag{11}$$

the equivalent impedance $z_{PV}(j\omega)$ can be simply expressed in Equation (12) as a function of the frequency [26].

$$z_{pv}(j\omega) = \left[R_s + \frac{R_p}{(\omega R_p C_p)^2 + 1}\right] - j\left[\frac{\omega R_p^2 C_p}{(\omega R_p C_p)^2 + 1}\right]. \tag{12}$$
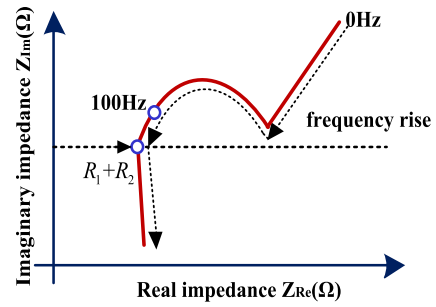
FIGURE 4. Nyquist plot of ac impedance with frequency rise.

The equivalent circuit model of a Li-ion battery is a combination of a voltage source, resistors, and capacitors. Its dynamics are described by an RC ladder circuit [27], as shown in Fig. 3(c), in which R_1 represents the series resistance, and R_2 and C_j are the resistance and capacitance of the RC ladder, respectively. The ac equivalent impedance can be expressed as:

$$z_{Li}(j\omega) = \left[R_1 + \frac{R_2}{(\omega R_2 C_j)^2 + 1}\right] - j\left[\frac{\omega R_2^2 C_j}{(\omega R_2 C_j)^2 + 1}\right]. \tag{13}$$

By observing (12)–(13), the current ripple can be evaluated by comparing the parameters of these models. When $\omega \rightarrow 200\pi$ (double-line-frequency $f_r = 100$ Hz), the impedances of the PV arrays and Li-ion batteries on the real axis tend to $R_s + R_p$ and $R_1 + R_2$, respectively. Normally, $R_s + R_p$ is much larger than $R_1 + R_2$ [28], [29]. Therefore, $|z_{PV}(200\pi)|$ (of the order of ohm) is much larger than $|z_{Li}(200\pi)|$ (of the order of 10 million). Based on the above quantitative analysis, it is clear that Li-ion batteries in EVs are more suitable for ripple power decoupling than PV arrays, with the current ripple injection control strategy.

D. SINUSOIDAL RIPPLE-CURRENT CHARGING/DISCHARGING

From the viewpoint of the electrical circuit, different charging frequencies will result in different battery AC impedances, based on the AC impedance model of the Li-ion battery, as interfered with by equation (13). Fig. 4 shows a Nyquist impedance plot obtained by calculating the impedance by frequency.

Obviously, the frequency-dependent battery impedance is minimized at high frequencies in the AC analysis. As a result, in [30], it was shown that the SRCC technique improves the charging time in comparison with the traditional constant current-constant voltage (CC-CV) charging. In particular, in the TPCS application, although the double-line frequency (100 Hz) is not the optimal frequency (approximate to 1000 Hz), which corresponds to the minimum AC impedance of batteries, the equivalent impedance $|z_{Li}(200\pi)|$ is much smaller than $|z_{Li}(0)|$, with traditional DC charging. Therefore, the energy loss in the battery charging/discharging

process can be reduced significantly, and the charge transfer efficiency improves.

As the aging effects of AC ripple current are concerned, SRCC has a negligible impact on the cycle-or calendar-life of Li-ion cells in most cases, when the amplitude of the sinusoidal ripple current is limited to 1C (capacity), as concluded from the study of Ref [31]. Additionally, as reported by Refs [32], [33], SRCC has the best charging/discharging performance, improving the charging time, charging efficiency, and lifetime of the battery.

Ref [34] studied the long-term impact of current ripple on battery performance degradation and comparative experiments with different charging strategies. According to the results of comparative experiments, the CC-CV's resultant capacity after 839 cycles is equal to that of the SRCC strategy after the mental result shows that 1000 cycles, with a constant average magnitude of the current ripple at 1C, constantly. This means that the lifetime is improved by approximately 16.1% using the SRCC strategy. Ref [35] investigated the functions of a sinusoidal waveform charging strategy and concluded that notably reviving aged batteries and prolonging battery cycle life can be achieved by utilizing SRCC for charging Li-ion batteries. Overall, although long-term tests on battery lifetime are certainly necessary, preliminary results show that the amplitude-limited double-line-frequency ripple charging current has a minor impact on the capacity and lifetime of Li-ion batteries.

E. REDUCTION OF DC-LINK CAPACITANCE WITH SRCC STRATEGY

Supposing λ is the ratio of dc-link voltage ripple, namely,

$$\lambda = \frac{u_r}{U_0}. \tag{14}$$

According to (7), the DC-link capacitance is [17]:

$$C = \frac{U_g I_g}{2\omega\lambda U_0^2}. \tag{15}$$

In the proposed 2.5 kVA TPCS, assuming that the rated dc-link is set to 360V, and $U_g = 311$V, the minimum value of the dc-link capacitance with the conventional passive decoupling approach is 6144uF, taking $\lambda = 1\%$. For the evaluation of the reduction of the DC-link capacitance with SRCC, a further study is shown in Fig.5, assuming a rated voltage of 250V of rated voltage, and 10Ah capacity for Li-ion batteries in the TPCS.

Fig. 5 demonstrates that the requirement of the dc-link capacitance can be decreased significantly with the SRCC technique. In extreme cases, no decoupling capacitance is needed when the coupling ripple power is absorbed by Li-ion batteries, and the AC amplitude is within the limit area of safety operations. However, according to the principle of dc/ac conversion, a small DC-link capacitance is still necessary for power balance and switching noise filtering.
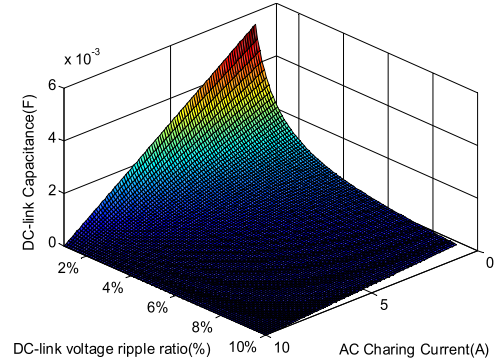

FIGURE 5. Requirement of dc-link capacitance as functions of dc-link voltage ripple and ac charging current for Li-ion batteries.

III. ACTIVE CONTROL STRATAGY FOR ALLEVIATING THE DC-LINK BUS VOLTAGE RIPPLE WITH SINUSOIDAL CHARGING/DIACHARGING

A. CONTROL SCHEME FOR V2G/G2V/PV2G OPERATION MODES IN TPCS

The general control scheme for V2G/G2V/PV2G operation modes, in which the grid is involved in the TPCS, is shown in Fig.6. In these operation modes, a direct power control algorithm was used. As the phase-locked loop (PLL) is adopted for the detection of the grid angle, the active and reactive powers p and q are expressed as

$$\begin{bmatrix} p \\ q \end{bmatrix} = \frac{1}{2} \begin{bmatrix} u_\alpha & u_\beta \\ -u_\beta & u_\alpha \end{bmatrix} \begin{bmatrix} i_\alpha \\ i_\beta \end{bmatrix}, \tag{16}$$

in α-β stationary coordinates based on the instantaneous power theory. where u_α, u_β and i_α, i_β are filtered, 90° phase delay for grid voltage u_g, and grid current i_g, respectively, by a second-order generalized integrator (SOGI). p_{ref}^* and q_{ref}^* are the active and reactive power commands, respectively, from the superior controller, according to the ancillary services for the smart grid. Two PI regulators were used for feedback control in the two power control loops. The active power command p_{ref}^* can be set to positive or negative to control the TPCS to inject or absorb active power from the grid. In addition, the reactive power command q_{ref}^* can be positive or negative, meaning that the TPCS provides the leading and lagging reactive power to the grid. The grid current reference i_g^* is derived using equation (17) when $i_g^* = i_\alpha^*$.

$$\begin{bmatrix} i_\alpha^* \left(i_g^* \right) \\ i_\beta^* \end{bmatrix} = \frac{2}{u_\alpha^2 + u_\beta^2} \begin{bmatrix} u_\alpha & -u_\beta \\ u_\beta & u_\alpha \end{bmatrix} \begin{bmatrix} p^* \\ q^* \end{bmatrix}. \tag{17}$$

Finally, the grid controller adopts a proportional-resonant (PR) controller:

$$G_{PR}(s) = K_{Pg} + \frac{K_{Rg}\omega s}{s^2 + \omega^2}, \tag{18}$$

where K_{Pg} and K_{Rg} are the proportional and resonant parameters, respectively, and ω is the grid fundamental angular frequency.

It is worth noting that, in the TPCS, DC-link capacitors are unsuitable as the power decoupling component, not only
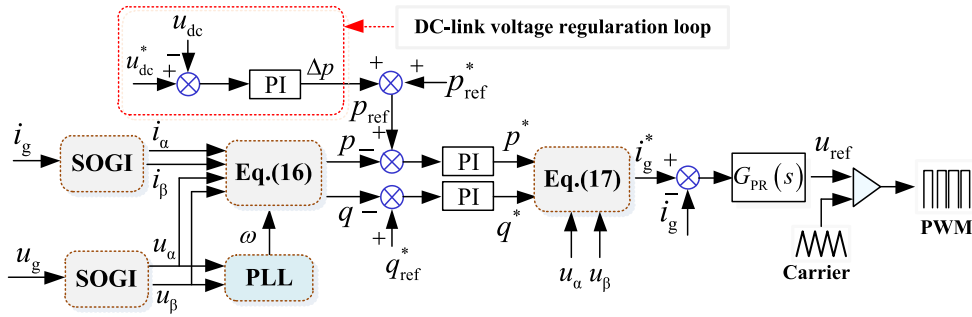
FIGURE 6. General control scheme of direct power control for TPCS.

for lifetime and volume reasons, but also because the DC-link voltage ripple will result in the reduction of AC power quality. As shown in Fig.6, the dc-link voltage is regulated by adding the active regulation power Δp to the power control loop, which is the sum of the active regulation power Δp, and the active power reference p_{ref}^* is expressed as

$$p_{\text{ref}} = p_{\text{ref}}^* + \Delta p. \tag{19}$$

However, if the DC-link voltage ripple is induced, the active power p^* will contain a double-line-frequency component. Then, the third-order harmonic is inducted in the grid current reference i_g^* by equation (17); thus, ac quality will be reduced.

B. CONTROLLER FOR INPUT CURRENT RIPPLE

To achieve power decoupling and allow ripple power to flow into the batteries completely, among the V2G/G2V/PV2G operation modes, the ripple component should be superposed into the current reference, and a sinusoidal charging/discharging current reference is formed. Meanwhile, in different operation modes, the current reference is derived from different control objectives.

1) The V2G operation mode, where the EVs provide ancillary services (providing active and reactive power) to the grid, and the current reference for the front-end bidirectional dc/dc converter i_{Bref}, can be derived from instantaneous grid power, assuming no power losses.

$$i_{\text{Bref}} = \frac{p_g}{U_B} = \frac{U_g I_g}{2U_B} \cos\varphi - \frac{U_g I_g}{2U_B} \cos(2\omega t - \varphi)$$
$$= I_{\text{dcB}} + i_{\text{rB}}, \tag{20}$$

where, $I_{\text{dcB}} = \frac{U_g I_g}{2U_B} \cos\varphi$, $i_{\text{rB}} = -\frac{U_g I_g}{2U_B} \cos(2\omega t - \varphi)$. The amplitudes of the grid voltage and current are easily obtained by Equation (21), and less delay is introduced.

$$\begin{cases} U_g = \sqrt{u_\alpha^2 + u_\beta^2} \\ i_g = \sqrt{i_\alpha^2 + i_\beta^2}. \end{cases} \tag{21}$$

Obviously, i_{Bref} is composed of two components, namely, the dc component I_{dcB}, to provide active

power, and the current ripple i_{rB}, for the decoupling power.

2) PV2G operation mode, in this mode, the active power in the grid is provided by the PV arrays through the front-end boost converter. Thus, the current reference i_{Bref} is to mitigate the DC-link voltage ripple in the form of a sinusoidal, as follows:

$$i_{\text{Bref}} = \frac{p_r}{U_B} = -\frac{U_g I_g}{2U_B} \cos(2\omega t - \varphi) = i_{\text{rB}}. \tag{22}$$

3) In the G2V operation mode, in this mode, the active power is delivered from the grid, and the battery charging energy determined by the grid current i_g and phase angle φ is calculated using the power manager system (PMS). The current reference i_{Bref} can be expressed by Equation (23), as defined in Fig.2.

$$i_{\text{Bref}} = -\frac{p_g}{U_B} = -\frac{U_g I_g}{2U_B} \cos\varphi + \frac{U_g I_g}{2U_B} \cos(2\omega t - \varphi)$$
$$= I_{\text{dcB}} + i_{\text{rB}}. \tag{23}$$

Overall, the target of the control strategy for the input current on the battery side is to track the current reference, i_{Bref}, for battery discharging or charging operation. The block diagram of the battery input current control scheme is shown in Fig.7(a). $D_B(s)$ is the duty ratio in the s-domain, $T(s)$ is the transfer function for the dc/dc converter, and a low-pass filter (LPF) is used to filter the switching noise. Because i_{Bref} is composed of a dc component and an ac component, and the sinusoidal component is introduced into the current control loops, a sufficiently high gain for the sinusoidal component at the double-line frequency should be fulfilled. A simple PI controller superposed by a resonant controller forms a PIR controller, as shown in Fig. 7(b), and the transfer function is expressed as:

$$H_i(s) = K_p + \frac{K_i}{s} + \frac{K_R \omega_0^2}{s^2 + 2\omega_c s + \omega_0^2}, \tag{24}$$

where K_p, K_i, and K_R are the proportional, integral, and resonant controller parameters, respectively, ω_c is the system resonance attenuation coefficient, and ω_0 is the resonance frequency, tuned to be synchronized at

(a)

(b)

(c)
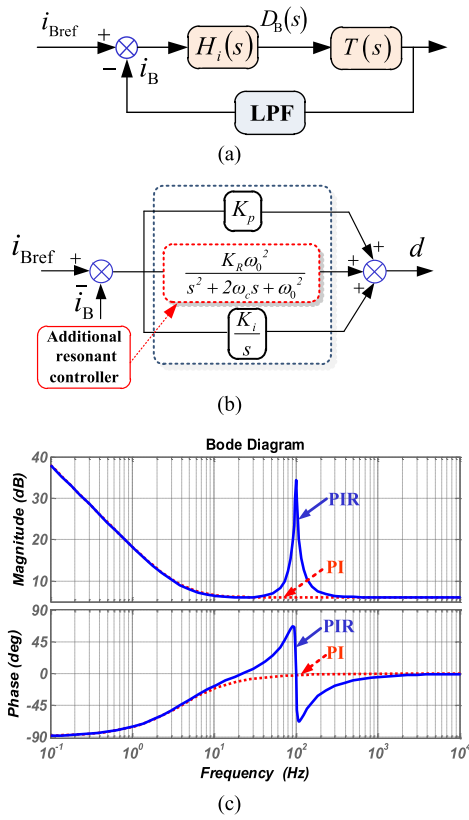
FIGURE 7. Close-loop control scheme and structure of PIR controller diagram for batteries' current, (a) close-loop control scheme, (b) structure of the PIR controller and (c) Bode diagram of the PIR controller.

the double-line frequency, namely, $\omega_0 = 2\omega$. Considering $K_p = 2$, $K_i = 50$, $\omega_c = 10$, and $K_R = 100$, the Bode diagram is shown in Fig. 7 (c). From the Bode diagram, it can be observed that the PIR controller has a high gain not only in the low-frequency band, but also at the resonant frequency ω_0. This reflects the inhibitory effect of the controller on the resonant ripple current and DC component.

C. PREDICTIVE CURRENT CONTROL

Focusing on the closed-loop current controller for the half-bridge PWM dc-dc converter, to compensate for the delay induced by the sensors, LPF, and PI regulator in $H_i(s)$, the predicted current control algorithm is proposed in Fig.8. Once the current references are obtained at *instant k*, they must be extrapolated to $k + 1$ instant; thus, the following fourth-order Lagrange extrapolation [36] can be used:

$$i_{Bref}(k+1) = 4i_{Bref}(k) - 6i_{Bref}(k-1) \\ + 4i_{Bref}(k-2) - i_{Bref}(k-3). \quad (25)$$

Then, the controller can predict the duty ratio $D'_B(k+1)$ for the $(k+1)$th cycle. Additionally, the controller can finely adjust the duty ratio based on the current difference between the predicted reference current $i_{Bref}(k+1)$ and the reference current $i_{Bref}(k)$ in k instant by parameter K_T.
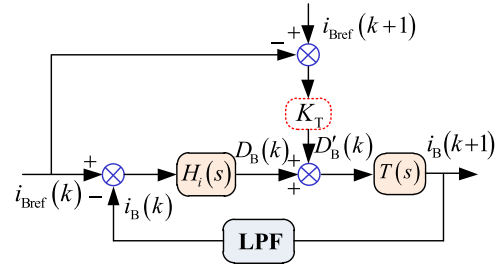
FIGURE 8. A control block diagram of the half-bridge PWM dc/dc with predict current algorithm.

IV. RESONANT COMPENSATE CONTROL SCHEME FOR DC-LINK VOLTAGE RIPPLE FURTHER MITIGATION METHOD

In the ideal case, assuming 100% conversion efficiency, all ripple power flows into the battery pack, and there is no voltage ripple in the DC link. However, some voltage ripple still remains in the DC-link because of imperfect implementation, such as the phase delay in the control loop. Moreover, if the ripple power, which is absorbed by the ac inductors L_1 and L_2 into account, the instantaneous ripple power of the coupling ac inductor is defined as p_{Lr}, assuming the grid inductor $L_g = L_1 + L_2$,

$$p_{Lr} = L_g i_g \frac{di_g}{dt} = \frac{1}{2}\omega L_g I_g^2 \sin(2\omega t - 2\varphi). \quad (26)$$

The actual ripple power p_{rA} transmitted to the DC link is in the grid current control loop. The actual lagged phase θ for ripple power can be calculated with the instantaneous grid voltage and grid current using Equation (27).

$$\begin{aligned} p_{rA} &= p_g - p_{Lr} - p_d \\ &= -\frac{1}{2}U_g I_g \cos(2\omega t - \varphi) - \frac{1}{2}\omega L_g I_g^2 \sin(2\omega t - 2\varphi) \\ &= P_{rA}\cos(2\omega t - \theta). \end{aligned} \quad (27)$$

Thus, the parameter drift of inductors may also result in voltage ripple remains in the DC-link, derived from equation (27).

In order to completely compensate the voltage ripple in the DC-link, which is caused by the power losses, non-ideal implementation, calculation errors, and parameter drift of inductors, it is necessary to adjust the amplitude and phase of the current reference in equations (20)-(22). Therefore, an additional closed-loop control, as shown in Fig.9, was induced to fulfill the full compensation condition.

In the additional closed loop, the voltage ripple reference $u_r^* = 0$, the voltage ripple error is regulated by the regulator $H_v(s)$,

$$H_v(s) = K_{vp} + \frac{K_{vR}\omega_0 s}{s^2 + \omega_0^2}, \quad (28)$$

where K_{vp} and K_{vR} are the proportional and resonant controller parameters, respectively. The output of regulator $H_v(s)$ is the adjusted value i_R, forming the new
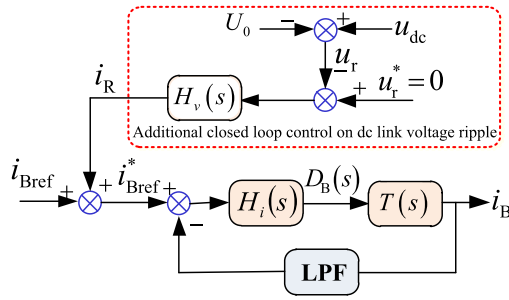
FIGURE 9. Close-loop control scheme for current controller with additional closed loop control on dc-link voltage ripple.
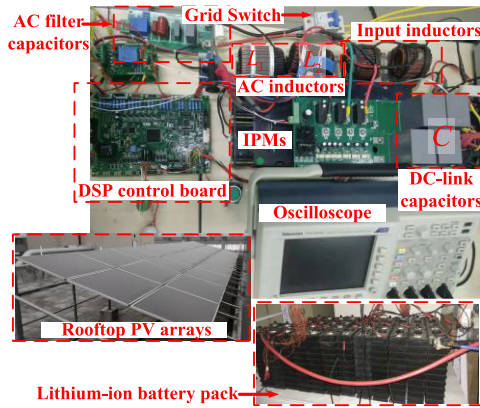

FIGURE 10. Experimental prototype of TPCS.

current reference i_{Bref}^*, by adding i_{Bref}, as shown in Fig.9 and equation (29).

$$i_{Bref}^* = i_{Bref} + i_R. \qquad (29)$$

V. EXPERIMENTAL RESULTS

The experimental prototype shown in Fig.10 was constructed to verify the performance of the power decoupling control method. The corresponding experimental parameters are presented in Table 1. In this prototype, an intelligent power module (IPM) integrating seven IGBTs, PM50RLA060 from MITSUBISHI, was used. The control of operation modes for TPCS was implemented by a Texas Instruments F28335 DSP-based platform. It is worth noting that electrolytic capacitors are replaced by four film capacitors (each capacitor is $50uF$) for the DC-link, and only $200uF$ is used in total. The Li-ion battery 3.25V in series, the nominal voltage of the battery pack is 243.75 V, pack is composed of 75 battery cells with nominal voltage, the actual output voltage is 245 V, and the nominal capacity is 15Ah, almost 1/6 of the practical battery capacity of EVs. The open-circuit voltage of the PV arrays was 250V, and the short-circuit current of the PV arrays was 12A.

A. V2G OPERTION MODE

Fig. 11 shows the grid voltage (u_g), grid current (i_g), discharging current of the battery pack (i_B), and dc-link voltage (u_{dc})
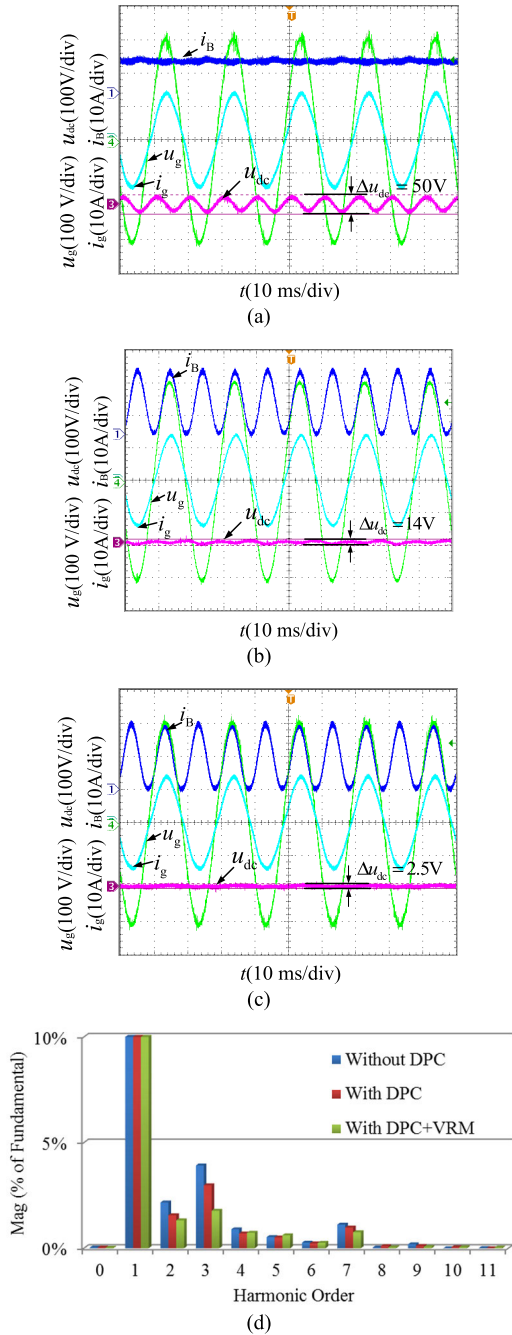
TABLE 1. Parameters of 2.5 kVA prototype.

Parameters	Value
Switching Frequency $\quad f_s$/Hz	20k
ac filter inductor $\quad L_1 = L_2$/mH	1.5
Input boost inductor L_{pv}/mH	2
Bidirectional dc/dc $\quad$ inductor L_B/mH	2
dc-link capacitor $\quad C/u$F	200
Rated Capacity $\quad S_e$/kVA	2.5
Output frequency $\quad f$/Hz	50
Rated out voltage $\quad u_{ac}$/V	220
Rated battery Pack Voltage u_B/V	245
Nominal capacity of battery Pack/Ah	15
PV open circuit voltage u_{op}/V	250
PV short circuit current i_{sc}/A	12
Rated dc-link Voltage u_{dc}/V	360

during the V2G operation mode for an operating power of 2.45 kW, with a power factor (PF) of unity. In Fig.11(a), the battery pack discharges dc energy (i_B = 10A current, output voltage u_B = 245V) to the grid without power decoupling control, and the ripple power is decoupled by the DC-link capacitors, and the DC-link voltage and ripple measurements are performed by applying an offset to channel 3, with ac coupling mode in the oscilloscope. From the waveforms in Fig.11(a), a 50V (peak-peak value) ripple in the DC-link voltage can be observed, without the power decoupling control, and the grid current is distorted. Fig. 11(b) shows the waveforms of the TPCS when it is working in the V2G operation mode, with PF = 1 and power decoupling control (PDC). It can be seen that the discharging current i_B becomes sinusoidal with the dc offset, decoupling most of the ripple power; thus, the DC-link voltage ripple is decreased to 14V. However, the ripple at 100 Hz is still exhibited in the DC-link voltage, indicating that the ripple power is not completely absorbed. To fully suppress the 100 Hz voltage ripple in the DC-link, a closed-loop control strategy for DC-link voltage ripple mitigation (VRM) is proposed in Part C of Section III, as shown in Fig. 11(c). The dc-link voltage ripple is further decreased, and only 2.5V (peak-peak value) is observed. Fig.11(d) illustrates the harmonic spectrum of the grid current i_g in Fig.11(a), Fig.11(b), and Fig.11(c). From the fast Fourier transform (FFT) analysis, the total harmonic distortion (THD) of i_g in the three experimental studies were 5.06%, 4.1%, and 2.98%, respectively. The AC power quality has been improved, and most harmonics especially the 3rd harmonic have been reduced in large quantities.

Fig.12 illustrates the results of the dynamic performance experiment for TPCS during the V2G operation mode, with PF = 1. In both the transients of sudden startup and sudden stand-by of the proposed active PDC + VRM control, TPCS can stabilize again in less than half of the power cycle. This

FIGURE 12. Dynamic transient responses with the proposed PDC + VRM: (a) sudden startup; (b) sudden stand-by.

inductive reactive power to the grid. Meanwhile, the ripple power decoupling function is illustrated in Fig.13(b), with the proposed ripple power decoupling control and voltage ripple mitigation algorithm. It can be seen that the DC-link voltage ripple is decreased dramatically, from 42V to 5V, in peak-peak value, by comparison of channel 3 of Fig.13(a) and Fig.13(b).

The harmonic spectrum of the grid current i_g in Fig.13(a)–(b) is illustrated in Fig.13(c), where the THD of i_g decreased from 3.02%, to 4.92%.

A similar result of the experiment is illustrated in Fig.14, where the TPCS operates in the V2G operation mode, providing capacitive reactive power to the grid, with PF = −0.8. With the proposed PDC + VRM control algorithms, the DC-link voltage ripple decreased to 6V from 42V. The same apparent power as that shown in Fig.10 is fed from the battery pack, with a sinusoidal discharging current offset by the 8A DC component, the ripple power decoupling function is obtained, the AC power quality is improved, and the THD of ig is decreased to 2.75%, from 4.81%.

B. PV2G

In the daytime, when solar radiation is abundant, PV energy is fed to the grid through the TPCS. Therefore, the battery pack implements the ripple power decoupling function during the PH2G operation mode. In this case, the validation capacitance film capacitors are used in the DC-link, 45V voltage ripple is measured in the TPCS, while $u_{pv} = 225$V, $i_{pv} = 9.25$A, and 2081 W active power feeds to the grid, with maximum power point tracking (MPPT). To suppress
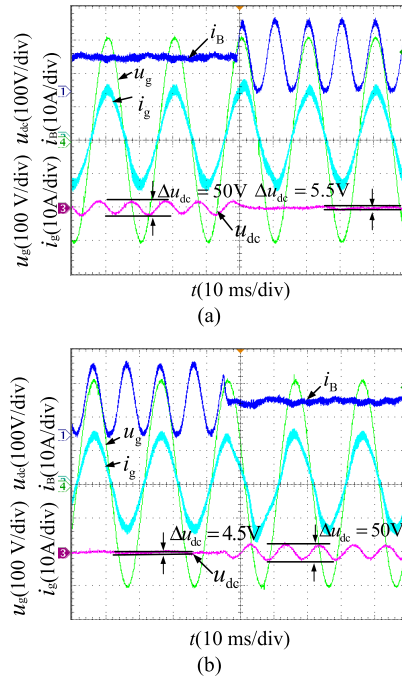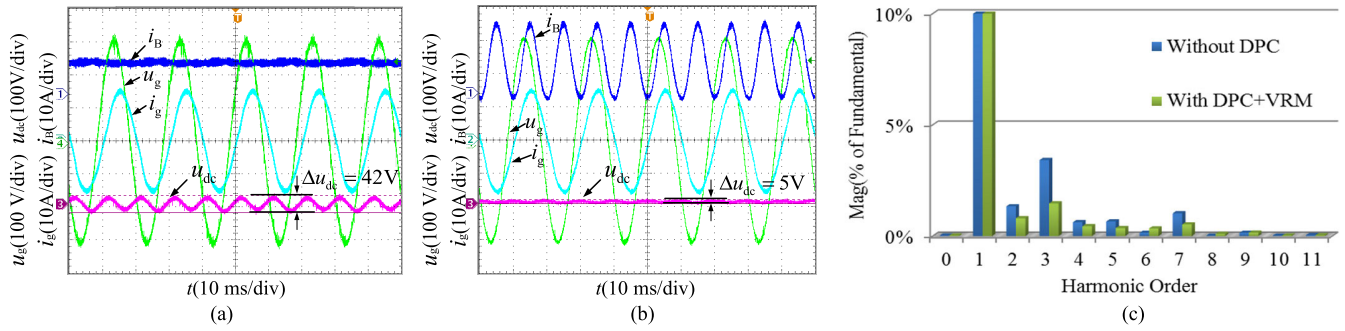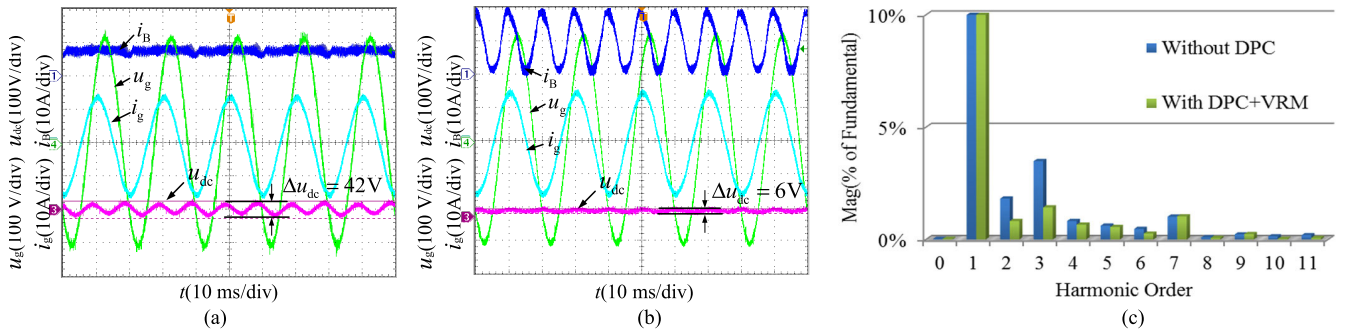

FIGURE 11. Experimental results during the V2G operation mode, with PF = 1: (a) without PDC; (b) with PDC; (c) with PDC + VRM; (d) harmonic spectrum of grid current of (a), (b) and (c).

means that a good dynamic performance can be ensured for the TPCS.

Fig.13 and 14 show the results of experimental validation studies for TPCS, which is working in V2G operation mode, providing active and reactive power to the grid. In Fig.13, the available energy in the battery feeds to the grid through TPCS, while providing inductive reactive power to the grid, with an apparent power of 2.2 kVA ($u_g = 220$V, $i_g = 10$A), PF = 0.8. The battery pack feeds 1.76 kW active power and 1.32 kVA

FIGURE 13. Experimental results during V2G operation mode, with PF = 0.8: (a) without PDC; (b) with PDC + VRM; (c) harmonic spectrum of grid current of (a) and (b).

FIGURE 14. Experimental results during V2G operation mode, with PF = −0.8: (a) without PDC; (b) with PDC + VRM; (c) harmonic spectrum of grid current of (a) and (b).
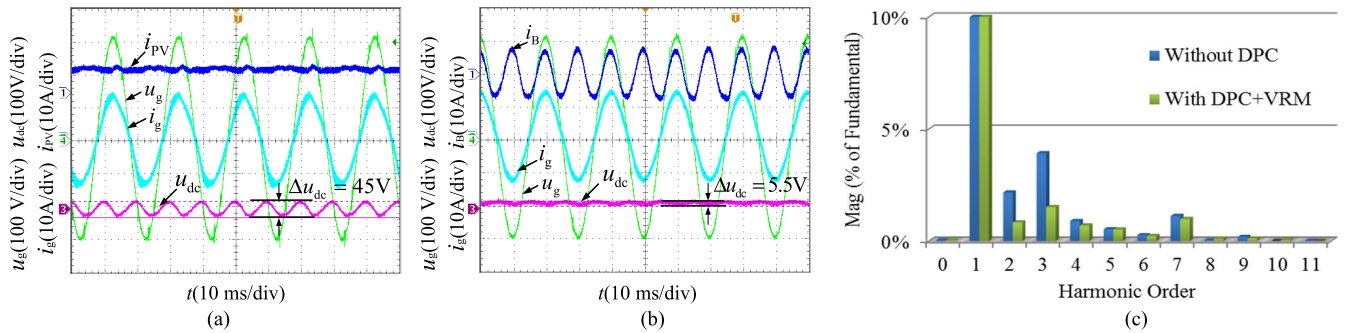
FIGURE 15. Experimental results during PH2G operation mode, with PF = 1: (a) without PDC; (b) with PDC + VRM; (c) harmonic spectrum of grid current of (a) and (b).
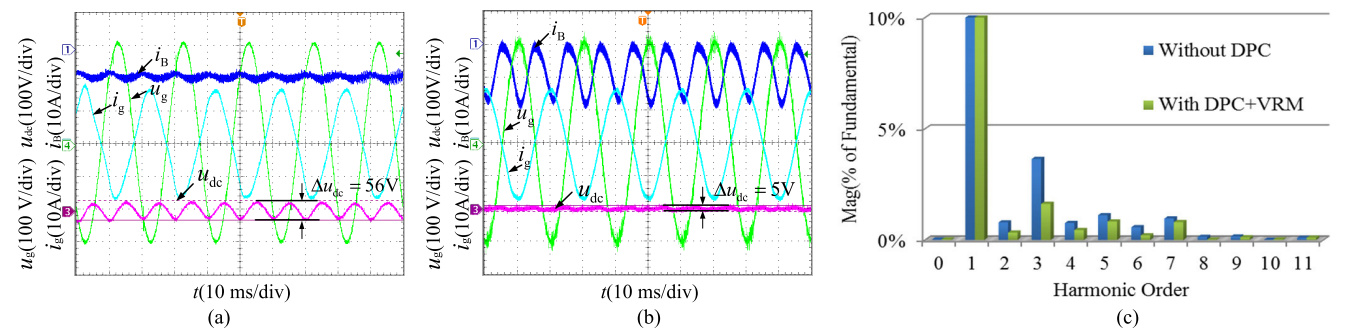

FIGURE 16. Experimental results during G2V operation mode, with PF = 1: (a) without PDC; (b) with PDC + VRM; (c) harmonic spectrum of grid current of (a) and (b).

the DC-link voltage ripple, the battery pack absorbs ripple power and provides zero active power. Fig.15(b) illustrates that the battery pack current i_B is sinusoidal without a dc offset, as shown in equation (21), decoupling the ripple power, and decreasing the voltage ripple. Only 5.5V voltage ripple can be observed in the dc-link, with more than a 2% decrease in the THD of the grid current i_g, from 5.21% to 2.98%.

C. G2V

Fig.16 shows the experimental waveforms of the TPCS during the G2V operation mode for an operating power of 2125W. During this operation mode, the grid current i_g is in the opposite phase with the grid voltage, and the TPCS draws the energy from the grid and charges the battery pack. Without active power decoupling control, the charging current iB is 8.5A, the battery terminal voltage is 245V, and the THD of the grid current is 5.16%. With the proposed control algorithm, the DC-link voltage ripple is significantly decreased from 56V to 5V, whereas the THD of the grid current is noticeably decreased to 2.88%.

VI. CONCLUSION

By interfacing PV arrays and batteries in electric vehicles, the single-phase TPCS is an essential element in future smart grids. To overcome the shortcomings of electrolytic capacitors, such as larger volume, short lifetime, and low reliability, the decoupling component should be reconsidered. Therefore, the equivalent ac impedance of the PV arrays and battery pack was modeled and analyzed. Based on a comparison of the equivalent AC impedance values of the PV arrays and battery pack, the impedance of the Li-ion battery pack in the double-line frequency is much lower than that of the PV arrays. Specifically, the former is only a few percent of the latter. Then, the mechanization of the reduction of the DC-link capacitance using the SRCC technique has been studied. Consequently, a Li-ion battery pack was selected as the optimal ripple power decoupling component to replace the electrolytic capacitor tanks in the PV/battery system. Moreover, power decoupling control with low DC-link capacitance has been proposed for V2G/G2V/PV2G operation modes for TPCS. To further eliminate the DC-link voltage ripple, improving the AC power quality in the grid, closed-loop control on the DC-link voltage ripple, with a resonant controller, was added. Finally, experimental results obtained from a 2.5 kVA prototype demonstrated the feasibility of the proposed PDC + VRM strategy. A more than 2% decrease in the THD of the AC grid current was achieved, even with a small dc-link capacitance. Compared to the traditional power decoupling method with DC charging, more than 90% capacitance can be saved in this study; thus, cost and volume can be significantly reduced, which gives the potential to achieve a very high power density. Additionally, if all conventional electrolytic capacitors are replaced by film capacitors, the lifetime expectancy can be improved by nearly four times. The advantages are at the expense of increasing the complexity of the battery manager system (BMS), system controller, and PMS, and a slight increase in power loss. Because the proposed power decoupling control scheme can make the bidirectional dc/dc converter absorb all the ripple power, the conduction loss in the bidirectional dc/dc converter will be slightly increased, which degrades the conversion efficiency slightly in the PV2G operation mode.

In future research, intelligent charging/discharging technology, with ripple power decoupling function, according to the battery state of charge (SOC) estimation, should be further evaluated and verified in a single-phase or three-phase unbalanced PV/battery hybrid system.

REFERENCES

[1] S.-A. Amamra and J. Marco, "Vehicle-to-grid aggregator to support power grid and reduce electric vehicle charging cost," *IEEE Access*, vol. 7, pp. 178528–178538, 2019.

[2] H. Liu, Y. Zhang, S. Ge, C. Gu, and F. Li, "Day-ahead scheduling for an electric vehicle PV-based battery swapping station considering the dual uncertainties," *IEEE Access*, vol. 7, pp. 115625–115636, 2019.

[3] M. J. E. Alam, K. M. Muttaqi, and D. Sutanto, "Effective utilization of available PEV battery capacity for mitigation of solar PV impact and grid support with integrated V2G functionality," *IEEE Trans. Smart Grid*, vol. 7, no. 3, pp. 1562–1571, May 2016.

[4] V. Chamola, A. Sancheti, S. Chakravarty, N. Kumar, and M. Guizani, "An IoT and edge computing based framework for charge scheduling and EV selection in V2G systems," *IEEE Trans. Veh. Technol.*, vol. 69, no. 10, pp. 10569–10580, Oct. 2020.

[5] C. Greer, D. A. Wollman, D. E. Prochaska, P. A. Boynton, J. A. Mazer, C. T. Nguyen, G. J. FitzPatrick, T. L. Nelson, G. H. Koepke, A. R. Hefner, and V. Y. Pillitteri, "NIST framework and roadmap for smart grid interoperability standards, release 3.0," U.S. Dept. Commer., Nat. Inst. Standards Technol., Gaithersburg, MD, USA, Tech. Rep. NIST SP-1108r3, 2014.

[6] C. Le Floch, E. C. Kara, and S. Moura, "PDE modeling and control of electric vehicle fleets for ancillary services: A discrete charging case," *IEEE Trans. Smart Grid*, vol. 9, no. 2, pp. 573–581, Mar. 2018.

[7] W. Wang and X. Ruan, "A modified reference of an intermediate bus capacitor voltage-based second-harmonic current reduction method for a standalone photovoltaic power system," *IEEE Trans. Power Electron.*, vol. 31, no. 8, pp. 5562–5573, Aug. 2016.

[8] B. Liu, G. Li, D. He, and Y. Chen, "DC and AC power quality control for single-phase grid-tied PEMFC systems with low DC-link capacitance by solution-space-reduced MPC," *IEEE Trans. Ind. Electron.*, early access, Jun. 10, 2021, doi: 10.1109/TIE.2021.3086729.

[9] M. A. Vitorino, L. F. S. Alves, R. Wang, and M. B. de Rossiter Correa, "Low-frequency power decoupling in single-phase applications: A comprehensive overview," *IEEE Trans. Power Electron.*, vol. 32, no. 4, pp. 2892–2912, Apr. 2017.

[10] Y. Sun, Y. Liu, M. Su, W. Xiong, and J. Yang, "Review of active power decoupling topologies in single-phase systems," *IEEE Trans. Power Electron.*, vol. 31, no. 7, pp. 4778–4794, Jul. 2016.

[11] Y. Tang, F. Blaabjerg, P. C. Loh, C. Jin, and P. Wang, "Decoupling of fluctuating power in single-phase systems through a symmetrical half-bridge circuit," *IEEE Trans. Power Electron.*, vol. 30, no. 4, pp. 1855–1865, Apr. 2015.

[12] B. Liu, Z. Zhang, G. Li, D. He, Y. Chen, Z. Zhang, G. Li, and S. Song, "Integration of power decoupling buffer and grid-tied photovoltaic inverter with single-inductor dual-buck topology and single-loop direct input current ripple control method," *Int. J. Elect. Power Energy Syst.*, vol. 125, Feb. 2021, Art. no. 106423.

[13] Y.-M. Chen and C.-Y. Liao, "Three-port flyback-type single-phase microinverter with active power decoupling circuit," in *Proc. IEEE Energy Convers. Congr. Expo.*, Sep. 2011, pp. 501–506.

[14] H. Valipour, G. Rezazadeh, M. R. Zolghadri, and N. Noroozi, "Electrolytic capacitor-less AC–DC LED driver with constant output current and PFC," in *Proc. 6th Power Electron., Drive Syst. Technol. Conf. (PEDSTC)*, Feb. 2015, pp. 107–112.

[15] Y. Qiu, L. Wang, H. Wang, Y.-F. Liu, and P. C. Sen, "Bipolar ripple cancellation method to achieve single-stage electrolytic-capacitor-Less high-power LED driver," *IEEE J. Emerg. Sel. Topics Power Electron.*, vol. 3, no. 3, pp. 698–713, Sep. 2015.

[16] Y. Zhou, H. Li, and H. Li, "A single-phase PV quasi-Z-source inverter with reduced capacitance using modified modulation and double-frequency ripple suppression control," *IEEE Trans. Power Electron.*, vol. 31, no. 3, pp. 2166–2173, Mar. 2016.

[17] B. Liu, L. Wang, D. Song, M. Su, J. Yang, D. He, Z. Chen, and S. Song, "Input current ripple and grid current harmonics restraint approach for single-phase inverter under battery input condition in residential photovoltaic/battery systems," *IEEE Trans. Sustain. Energy*, vol. 9, no. 4, pp. 1957–1968, Oct. 2018.

[18] Y. M. Chen, H. C. Wu, Y. C. Chen, K. Y. Lee, and S. S. Shyu, "The AC line current regulation strategy for the grid-connected PV system," *IEEE Trans. Power Electron.*, vol. 25, no. 1, pp. 209–218, Jan. 2010.

[19] A. Choudhury, P. Pillay, and S. S. Williamson, "DC-link voltage balancing for a three-level electric vehicle traction inverter using an innovative switching sequence control scheme," *IEEE J. Emerg. Sel. Topics Power Electron.*, vol. 2, no. 2, pp. 296–307, Jun. 2014.

[20] T.-H. Kim, J.-B. Jeong, B.-H. Lee, D.-H. Shin, H.-S. Song, B.-H. Kim, and H.-J. Kim, "Analytical study on low-frequency ripple effect of battery charging," in *Proc. IEEE Vehicle Power Propuls. Conf.*, Oct. 2012, pp. 809–811.

[21] H. Z. Z. Beh, G. A. Covic, and J. T. Boys, "Effects of pulse and DC charging on lithium iron phosphate (LiFePO$_4$) batteries," in *Proc. IEEE Energy Convers. Congr. Expo.*, Sep. 2013, pp. 315–320.

[22] A. Bessman, R. Soares, S. Vadivelu, O. Wallmark, P. Svens, H. Ekström, and G. Lindbergh, "Challenging sinusoidal ripple-current charging of lithium-ion batteries," *IEEE Trans. Ind. Electron.*, vol. 65, no. 6, pp. 4750–4757, Jun. 2018.

[23] C. Lebron, F. Andrade, E. O'Neill, and A. Irizarry, "An intelligent battery management system for home microgrids," in *Proc. IEEE Power Energy Soc. Innov. Smart Grid Technol. Conf. (ISGT)*, Sep. 2016, pp. 1–5.

[24] M. Su, P. Pan, X. Long, Y. Sun, and J. Yang, "An active power-decoupling method for single-phase AC–DC converters," *IEEE Trans. Ind. Informat.*, vol. 10, no. 1, pp. 461–468, Feb. 2014.

[25] P. T. Krein, R. S. Balog, and M. Mirjafari, "Minimum energy and capacitance requirements for single-phase inverters and rectifiers using a ripple port," *IEEE Trans. Power Electron.*, vol. 27, no. 11, pp. 4690–4698, Nov. 2012.

[26] J. Johnson, D. Schoenwald, S. Kuszmaul, J. Strauch, and W. Bower, "Creating dynamic equivalent PV circuit models with impedance spectroscopy for arc fault modeling," in *Proc. 37th IEEE Photovoltaic Spec. Conf.*, Jun. 2011, pp. 2328–2333.

[27] D. Jiani, W. Youyi, and W. Changyun, "Li-ion battery SOC estimation using particle filter based on an equivalent circuit model," in *Proc. 10th IEEE Int. Conf. Control Autom. (ICCA)*, Jun. 2013, pp. 580–585.

[28] K. A. Kim, G.-S. Seo, B.-H. Cho, and P. T. Krein, "Photovoltaic hot-spot detection for solar panel substrings using AC parameter characterization," *IEEE Trans. Power Electron.*, vol. 31, no. 2, pp. 1121–1130, Feb. 2016.

[29] W. Kim, V.-H. Duong, T.-T. Nguyen, and W. Choi, "Analysis of the effects of inverter ripple current on a photovoltaic power system by using an AC impedance model of the solar cell," *Renew. Energy*, vol. 59, pp. 150–157, Nov. 2013.

[30] S.-Y. Cho, I.-O. Lee, J.-I. Baek, and G.-W. Moon, "Battery impedance analysis considering DC component in sinusoidal ripple-current charging," *IEEE Trans. Ind. Electron.*, vol. 63, no. 3, pp. 1561–1573, Mar. 2016.

[31] A. Bessman, R. Soares, O. Wallmark, P. Svens, and G. Lindbergh, "Aging effects of AC harmonics on lithium-ion cells," *J. Energy Storage*, vol. 21, pp. 741–749, Feb. 2019.

[32] M. Uno and K. Tanaka, "Accelerated charge-discharge cycling test and cycle life prediction model for supercapacitors in alternative battery applications," in *Proc. IEEE Intelec.*, Sagamihara, Japan, Oct. 2011, pp. 1–6.

[33] X. Wang, Y. Sone, H. Naito, C. Yamada, G. Segami, and K. Kibe, "Cycle-life testing of large-capacity lithium-ion cells in simulated satellite operation," *J. Power Sources*, vol. 161, no. 1, pp. 594–600, Oct. 2006.

[34] L.-R. Chen, S.-L. Wu, D.-T. Shieh, and T.-R. Chen, "Sinusoidal-ripple-current charging strategy and optimal charging frequency study for Li-ion batteries," *IEEE Trans. Ind. Electron.*, vol. 60, no. 1, pp. 88–97, Jan. 2013.

[35] P. Chen, F. Yang, Z. Cao, J. Jhang, H. Gao, M. Yang, and K. D. Huang, "Reviving aged lithium-ion batteries and prolonging their cycle life by sinusoidal waveform charging strategy," *Batteries Supercaps*, vol. 2, no. 8, pp. 673–677, Aug. 2019.

[36] O. Kukrer, "Discrete-time current control of voltage-fed three-phase PWM inverters," *IEEE Trans. Power Electron.*, vol. 11, no. 2, pp. 260–269, Mar. 1996.

ZHIGANG ZHANG received the Ph.D. degree from the College of Hydropower Engineering, Sichuan University, Chengdu, in 2010. Since 2018, he has been a Full Professor with the School of Management Science and Engineering, Guangxi University of Finance and Economics. His research interests include the optimal dispatching of power systems, modeling and control, and power engineering project management.

BIN LIU received the Ph.D. degree from the School of Information Science and Engineering, Central South University, Changsha, China, in 2014.

Since 2015, he has been an Associate Professor with the School of Electrical Engineering, Guangxi University. His research interests include the general area of power electronics and energy conversion, with particular emphasis on converter topologies, and modeling and control.

SHAOJIAN SONG received the B.S. degree in industrial electrical automation and the M.S. degree in control theory and control engineering from Guangxi University, Nanning, China, in 1994 and 2001, respectively. He is currently a Professor with the School of Electrical Engineering, Guangxi University. His current research interests include modeling, optimization and control for complex systems, electric vehicle, and V2G.

• • •